Materials Advances

ROYAL SOCIETY OF CHEMISTRY

PAPER

View Article Online
View Journal | View Issue

Cite this: *Mater. Adv.*, 2025, 6, 331

Doping functional ions in phase-stabilizing core–shell biphasic granules readily tunes bone regeneration *in situ*

Yan Xu,†[a] Jian Shen, †[b] Lingling Dong,[c] Xiaoyi Jiao,[d] Lei Zhang,[d] Jiaqi Yang,[a] Shanxiang Xu,[b] Xianyan Yang,[a] Huiming Zhong, *[b] Guoli Yang*[c] and Zhongru Gou*[a]

Some silicate- and phosphate-based bioactive ceramics exhibit excellent biocompatibility and undergo biodegradation to different extents, thereby attracting extensive attention and showing application in the field of bone tissue engineering. Moreover, functional ion doping is a versatile strategy for optimizing the performance of bioceramics. Herein, we developed a series of core–shell bio-ceramic granules, with zinc-doped wollastonite (CSi–Zn) as the core and tricalcium phosphate (TCP) or sodium-doped tricalcium phosphate (TCP–Na) as the shell, using a coaxial dual-nozzle system. The thickness ratio of the core and shell layers was finely controlled as 2 : 1 or 1 : 1. An *in vitro* immersion test demonstrated that the core–shell structure and functional ion doping could tailor the ion release behavior and granule dissolution in tris buffer, and the CSi component readily induced biomimetic re-mineralization in simulated body fluids. Critical size femoral bone defect repair experiments indicated that when the core–shell thickness ratio was 1 : 1, CSi–Zn@TCP granules exhibited superior bone repair performance at 18 weeks of post-implantation. This advantage was also particularly significant in the early stages (8 weeks) of post-implantation. Altogether, the tunable composition and structure of granule biomaterials offer excellent flexibility and feasibility, with the potential for the development of a series of derivative and variant products to address various clinical requirements.

Received 7th September 2024,
Accepted 24th November 2024

DOI: 10.1039/d4ma00911h

rsc.li/materials-advances

1. Introduction

Bone, a crucial organ in the human body, performs functions such as support, hematopoiesis, and protection of internal organs. It is capable of continuous self-renewal and improvement, with inherent repair and regenerative capabilities.[1,2] However, this regeneration and repair are not always perfect, especially when the bone defect exceeds its critical size.[3] Current common clinical bone repair treatments include autografts, allografts, and xenografts. However, these methods usually suffer from insufficient available bone quantity, donor site morbidity, disease transmission, or immune rejection.[4–7] Bone regenerative medicine, which emerged as a new research field more than two decades ago, has since attracted much attention and research.

Bone regenerative medicine is based on the understanding of tissue regeneration and formation and aims to cultivate new functional tissues *via* implanted artificial biomaterials.[8,9] Ideal biomaterials for bone repair should possess appropriate biodegradability, suitable porous architectures and structural maintenance.[10–12] It is known that Ca plays a critical role in normal bone growth and strengthening and is essential for the normal functioning of muscles and blood vessels.[13] Ca also promotes the adhesion and proliferation of osteoblasts, facilitating bone regeneration and repair.[14] Meanwhile, it is well known that the human body contains about 2% Ca, of which 98% is stored in the bones. The P element mainly exists in the form of phosphate in the human body, which is essential for a variety of physiological processes, and adequate phosphate is indispensable in the normal growth and development of bone.[15,16] Zn, a trace element, is essential for DNA synthesis, osteogenic cell division, and protein synthesis.[17] Moreover, Si

[a] *Bio-nanomaterials and Regenerative Medicine Research Division, Zhejiang-California International Nanosystems Institute, Zhejiang University, Hangzhou 310058, China. E-mail: zhrgou@zju.edu.cn; Tel: +86-571-8697-1539*
[b] *Department of Emergency Medicine, Second Affiliated Hospital, Zhejiang University School of Medicine, Key Laboratory of The Diagnosis and Treatment of Severe Trauma and Burn of Zhejiang Province, Zhejiang Province Clinical Research Center for Emergency and Critical Care Medicine, Hangzhou, Zhejiang 310009, China. E-mail: 20918332@zju.edu.cn*
[c] *Department of Implantology, Stomatology Hospital, School of Medical, Zhejiang University, Yan'an Road, Hangzhou, P. R. China. E-mail: guo_li1977@aliyun.com*
[d] *Department of Orthopaedic Surgery, The First Affiliated Hospital of Wenzhou Medical University, Wenzhou 325000, China*
† Co-first authors.

directly participates in the mineralization process of bones,[18] promoting the proliferation and differentiation of bone marrow mesenchymal stem cells and the repair of bone tissue at the site of injury.[19–21] Therefore, it is promising to develop a bioactive implant with these inorganic mineral elements for bone repair.

At present, the common bone defect repair bioactive materials mainly include some biodegradable metals, bioceramics and (biomimetic) composite materials. Biodegradable metals and alloys are primarily used as bone implants in areas subject to heavy mechanical loads but also suffer from issues such as stress shielding and burst release of some bioactive ions. For example, magnesium alloys have been used in orthopedics due to their superior biodegradation and high strength, yet they exhibit relatively fast H_2 release.[22,23] Common calcium phosphate and calcium or calcium–magnesium silicate biomaterials include hydroxyapatite (HA), tricalcium phosphate (TCP), wollastonite ($CaSiO_3$; CSi), akermanite ($Ca_2MgSi_2O_7$) ceramics, and bioactive glasses. HA closely resembles the mineral composition of natural bone, offering excellent bone conduction but low solubility and poor fracture toughness.[24,25] TCP bioceramics, with a Ca/P ratio (1.5 : 1) close to that of bone mineral, exhibit appropriate biodegradability and osteoconductive potential.[26–28] Geng *et al.*[29] coated TCP bioceramic onto a three-dimensional porous magnesium scaffold, demonstrating good cell adhesion and proliferation, indicating its potential as a bone tissue engineering scaffold material. Unfortunately, TCP bioceramics also have the drawback of poor sintering property and insufficient mechanical resistance. In contrast, CSi, a highly biodegradable ceramic, exhibits excellent bioactivity. It can tightly bond with bone, and the released bioactive ions can promote the proliferation, differentiation, and repair of bone tissue. Nowadays, CSi has been widely concerned and applied in the field of bone repair. It can be made into porous scaffolds[30] and combined with other materials,[31] showing various applications, whereas it also suffers from low mechanical strength and too fast biodegradation.

Furthermore, many researchers have employed various optimization and modification methods to address the inherent limitations in sintering, biodegradation and/or structural properties and biological performances of TCP and CSi bioceramics, with biphasic mixing or exogenous functional ion doping and composite modification.[32–34] In general, one or two properties of single components could be improved by introducing the secondary component, whereas the other properties were compromised with a common mechanical mixing approach. In particular, some composite preparation strategies have uncontrollable ion release, and it is reasonable to assume that the inflammatory reaction could occur at the interface of material and host tissue because of the spontaneous separation of ultrafine sparingly dissolvable granules.[35,36] Some biologically functional ions such as Sr,[37] Mg,[38] and Zn are frequently doped into the bioceramics. For example, Zn-doped CSi may improve the bone integration of implants in osteoporotic rabbits and promote new bone formation.[39] Moreover, the incorporation of Zn ions can improve the sintering and mechanical strength of the CSi bioceramic and promote osteogenic differentiation.[40–42] For the issue of TCP's brittle nature, some studies have shown that sodium doping can effectively enhance its sintering property without altering its bioactivity.[43,44] Recently, we have developed the core–shell assembly of CSi and TCP using a coaxial dual-nozzle system to prepare bioceramic microspheres.[45] This core–shell structure offers more precise and accurate control over the distribution and proportion of bioceramic components, as well as greater flexibility and diversity in the microporous structure using porogens.[46] Unfortunately, the conventional dissolvable calcium salt solution as a bioceramic slurry microsphere-collecting carrier readily leads to phasic conversion from TCP to the TCP/HA composite in the shell layer. Furthermore, the microporous structure of a completely coated shell layer would inhibit the biodegradation of the core component. These problems are inevitable to affect the biological performances of the multiphasic composite.[47,48]

Based on the above-mentioned concerns, the present study aims to develop a new shell-component phasic stability strategy and investigate the potential physicochemical properties and biological performances of selective functional ion doping in the core and shell component. Generally, Zn and Na ions were employed to respectively dope into CSi and TCP, and the core–shell bioceramic granules with a controllable core and shell thickness were prepared. We systematically evaluated the microstructure, *in vitro* ion release and *in vivo* osteogenic behavior of the core–shell fiber-derived bioceramic granules. The results indicated that the structural and composition design of such biphasic composite biomaterials facilitates precise control of their degradation both *in vivo* and *in vitro*, enabling highly efficient bone regeneration and repair. This study is beneficial for understanding the relationship between the component distribution, phasic stability, and bone tissue repair of core–shell bioceramic materials.

2. Experiments and methods

2.1 Reagents and materials

Sodium metasilicate nonahydrate ($Na_2SiO_3{\cdot}9H_2O$), zinc nitrate hexahydrate ($Zn(NO_3)_2{\cdot}6H_2O$), diammonium hydrogen phosphate ($(NH_4)_2HPO_4$), sodium dihydrogen phosphate (NaH_2PO_4), magnesium nitrate hexahydrate ($Mg(NO_3)_2{\cdot}6H_2O$), and ammonia solution (NH_4OH) were all of analytical grade. Calcium nitrate tetrahydrate ($Ca(NO_3)_2{\cdot}4H_2O$) had a purity of 98.5%. These reagents were purchased from Sinopharm Chemical Reagent Co., Ltd. Tris(hydroxymethyl)aminomethane (tris; purity $\geq$99.9%), carboxylated chitosan (CC), carboxymethyl cellulose (CMC), and anhydrous ethanol (C_2H_5OH) were obtained from Shanghai Aladdin Biochemical Technology Co., Ltd. Sudan III ($C_{22}H_{16}N_4O$; biotechnology grade) was purchased from Shanghai Macklin Biochemical Co., Ltd. All reagents were used as received without further purification.

2.2 Bioceramic powder synthesis

CSi with 5% Zn (CSi–Zn) and TCP (β phase) without and with Na-doping (TCP and TCP–Na, respectively) were synthesized *via*

a conventional chemical precipitation method.[49] TCP–Na was prepared by partially replacing diasmmonium hydrogen phosphate with sodium dihydrogen phosphate (1.0%) with the other conditions remaining the same. The calcined bioceramic powders were mixed with anhydrous ethanol and ball-milled with zirconia balls at 300 rpm for 6 hours to obtain the desired ultrafine powders.

2.3 Core–shell fiber-derived granule preparation

The liquid component for bioceramic fiber preparation consisted of a mass ratio of 2 : 1 of 7.0 wt% CC and 1.2 wt% CMC aqueous solutions. The bioceramic slurries were prepared with various bioceramic powders in a liquid medium, with a liquid-to-solid ratio of 1 : 1. These slurries were all mixed and stirred for 4 hours using a magnetic stirrer to obtain a desired bioceramic slurry. After that, each group of slurry (CSi–Zn core, TCP shell or TCP–Na shell) was sieved and transferred into a 10 ml syringe, respectively. The coaxially aligned 21G/16G nozzles (∅ 0.5 mm, ∅ 1.2 mm) allowed the different slurries to be extruded from separate channels, forming a core–shell structured fiber (Fig. 1). The different extrusion speeds controlled by the pressure differences allowed for varying the thickness ratio (2 : 1 and 1 : 1) of core and shell layers. Incidentally, a small amount of Sudan III was added to the core slurry as a colorant for easy differentiation. After the fibrous slurry flowed out of the nozzle, the magnesium salt solution with a concentration of 1.3 M was obtained. Mg^{2+} in the collecting solution would chelate with the carboxyl group in CC in the fibrous slurry, fixing the fiber morphology. After immersion in the solution for 12 hours, the fibers were dried in an oven at 60 °C, and followed by cutting into short fibers (*i.e.* granules) of the desired length (~1.2–1.5 mm). Finally, the granules were sintered in a muffle furnace at 1150 °C for 2 hours. Using this method, four groups of core–shell bioceramic granules were prepared according to the core–shell component and thickness ratios (denoted as CSi–Zn@TCP (2 : 1), CSi–Zn@TCP (1 : 1), CSi–Zn@TCP–Na (2 : 1), and CSi–Zn@TCP–Na (1 : 1)). Additionally, a fifth group, CSi–Zn/TCP–Na, was prepared by mechanically mixing CSi–Zn and TCP–Na powders in a mass ratio of 1/1, while the preparation method remained the same.

2.4 Chemical composition and phase analysis

The synthesized powders and granules were characterized by X-ray diffraction (XRD) with CuKα radiation at a scanning speed of 2° min^{-1} from 5° to 80° of angular range. Inductively coupled plasma-optical emission spectroscopy (ICP-OES) was used to quantitatively determine the ion content in the bioceramic powders and ion release from the granules.

2.5 Sintering potential evaluation of Na doping in TCP

The improvement in the sintering properties of TCP without and with Na doping was analyzed using a microcomputer-controlled electronic universal material testing machine (WD-T type). A certain amount of powder was uniformly mixed with an appropriate amount of 4 wt% polyethylene glycol solution, placed in a mold, and pressed into a rectangular shape using a DY-20 desktop electric press. The samples were then calcined in a muffle furnace at 1150 °C for 2 hours. The length and width of the plates were measured, and the temperature and humidity during the experiment were recorded. The stress–strain curve data during the experiment were acquired using the AnyTest Standard software (Version: 2.13.37.97). Each measurement was repeated three times to get the average value.

2.6 Morphological and microstructural analyses of granules

The macroscopic morphology of the bioceramic granules was determined and characterized using calipers and a mobile camera. The microscopic structures of bioceramic granules were observed using a scanning electron microscope (SEM), and the micro-area elemental composition of the granule cross-sections was evaluated using an energy-dispersive spectrometer (EDS).

2.7 Evaluation of *in vitro* biodegradation and re-mineralization of granules

The bioceramic granules were immersed in a tris–HCl buffer (pH ~ 7.4) and placed in a constant temperature incubator at 37 °C to simulate ion release and biodegradation *in vitro*. For the ion release evaluation, 0.10 g granules were immersed in 10 ml of Tris buffer. After soaking for 1, 3, 5, 7, 14, and 28 days, 1 ml of the supernatant was extracted and diluted with 9 ml of deionized water, and the ion concentrations of Zn, Ca, Si, Na, P, and Mg were measured using ICP-OES. Meanwhile, 1 ml of fresh buffer was added to the immersion solution to balance the buffer volume. The mass decay tests of the granules were conducted following a similar procedure. Then 0.30 g of granules were immersed in 10 ml of Tris buffer. After soaking for 1, 2, 3, 4, 6, 8, and 12 weeks, respectively, the granules were

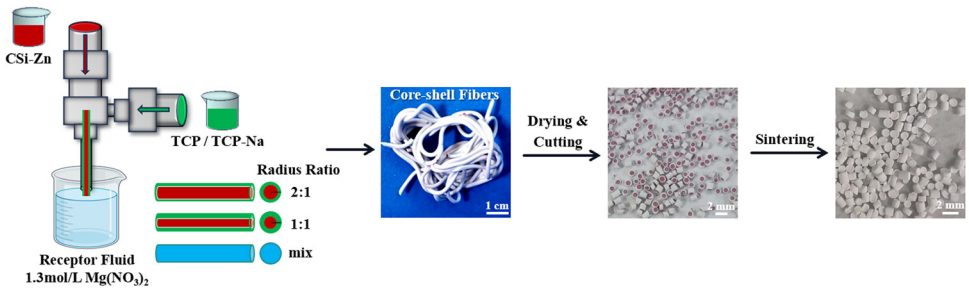

Fig. 1 Preparation process of core–shell selective regionally ion-doped bioceramic granules.

removed, washed sequentially with deionized water and anhydrous ethanol, and then dried in an oven at 80 °C. They were weighed and recorded when the mass was constant. Each experiment was repeated three times to minimize the random error.

To study the *in vitro* re-mineralization potential, the bioceramic granules were immersed in simulated body fluids (SBFs) and placed in a constant temperature incubator at 37 °C. Specifically, 0.10 g of granules were immersed in 10 ml SBF. After soaking for 7 and 14 days (with 20% of SBF being refreshed every two days), the granules were removed, washed three times with deionized water and anhydrous ethanol, and dried in an oven at 80 °C. The induced apatite re-mineralization capability of the granules was then characterized using SEM and EDS.

2.8 *In vivo* osteogenesis capability of the granules

2.8.1 Granule implantation. This study was officially approved by the Ethics Committee for Experimental Animals at Zhejiang University (ZJU20220475). Twenty male New Zealand white rabbits, each weighing between 2.8 and 3.0 kg and averaging 4 months old, were selected for femoral condyle implantation experiments. The rabbits were randomly divided into five groups, each receiving one of the five different implantation materials, with four rabbits per group. Anesthesia was administered by injecting 3% pentobarbital sodium into the marginal ear vein at a dose of 1.0 mg kg^{-1}. A critical-sized cylindrical bone defect ($\varnothing \sim 6 \times 7$ mm) was created in the lateral femoral condyle using a dental ring ($\varnothing$ 6 mm), and the defect was filled with the bioceramic granules (diameter: 0.85 ± 0.05 mm; height: 1.5 ± 0.3 mm). The incision was sutured layer by layer, and a certain amount of penicillin powder was applied to prevent infection. Postoperative care included a daily intramuscular injection of penicillin (800 000 U) for three consecutive days. After 8 and 18 weeks of rearing, respectively, the rabbits were euthanized by intravenous injection of an overdose of pentobarbital sodium, and bone specimens were collected for subsequent analyses.

2.8.2 X-ray and μCT analysis. X-ray imaging (XPERT; KUBTEC Co., USA) was performed under conditions of 40 kV and 3.2 mA to capture anteroposterior and lateral views of the rabbit femoral specimens, providing preliminary insights into bone growth and material degradation at the defect site. Further assessment of new bone growth and distribution was conducted using a μCT imaging system (AX2000 CT scanner, Always Imaging, Shanghai). At room temperature, X-ray scanning was performed along the anatomical axis of the femur (microfocus X-ray source: FineTec 160 kV, Germany; X-ray detector: NDT 1717M, pixel size: 139 μm, pixel number: 3072 × 3072, voxel size: 14 μm), generating continuous cross-sectional images (image resolution: 15.6 μm; exposure time: 500 ms). Specialized software was then used to reconstruct three-dimensional images. The region of interest (ROI; $\varnothing \sim 6 \times 7$ mm) was centered on the fracture, and quantitative analysis was performed based on density differences to distinguish new bone tissue and implanted materials within the ROI. Bone trabecular morphologic parameters including bone volume fraction (BV/TV), material volume fraction (RV/TV), and mean trabecular number (Tb.N; 1 mm^{-1}) were calculated using VG Studio MAX.

2.8.3 Histological analysis. The femoral specimens were immersed in a 4% formaldehyde solution for at least one week for fixation, and then rinsed with pure water. They were sequentially dehydrated using graded ethanol (80–100%), followed by xylene washing, and finally embedded in polymethyl methacrylate. Using a sectioning machine (SP1600, Leica, Germany), cross-sectional slices of the cylindrical bone defect were cut, producing 8–10 slices per specimen. These slices were then polished using a polishing machine (MP-2B). The sections were stained with hematoxylin and eosin (H&E) and Masson's trichrome stain, and the area of newly formed bone tissue was quantitatively assessed using the IPP6.0 software to determine the percentage of newly formed bone tissue (BS/TS%).

2.9 Statistical analysis

All data are expressed in the form of mean ± standard deviation (SD). Some quantitative data were analyzed using one-way analysis of variance (ANOVA), with $p < 0.05$ representing statistical significance. Statistical analyses were performed using the Origin 2018 software (OriginLab Corporation, Northampton, Massachusetts, USA).

3. Results

3.1 Preliminary analysis and characterization

Fig. 1 illustrates the preparation and the outward appearance of biphasic bioceramic fiber-cut granules. Evidently, the bi-nozzle could readily produce bioceramic slurry fibers and the as-cut granules exhibited core–shell structures based on the assistance of colorant (Sudan III) in the core slurry component.

Fig. 2 shows the phasic composition, sintering and changes in the granule size of the bioceramic powders and granules. As shown in Fig. 2(A), the synthesized CSi–Zn powder corresponded to a pure wollastonite phase (PDF#27-0088). A slight peak shift was observed at 29.991°/2θ, which may be attributed to the substitution of Ca with Zn in the CSi structure. This shift indicates that Zn ions have partially entered the lattice, replacing Ca ions, and demonstrates that Zn doping does not significantly alter the overall structure of CSi. The XRD pattern of the TCP powder corresponds to the standard pattern for β-tricalcium phosphate (PDF#09-0169). For the TCP–Na powder, there is a subtle peak shift at 31.026°/2θ. The possible reasons for this result is that, on the one hand, the Na dopant is relatively low, which leads to fewer Na ions entering the lattice, and on the other hand the ionic radii of Na^+ and Ca^{2+} are quite similar, so the lattice distortion caused by Na^+ replacing Ca^{2+} is low, resulting in the observed slight peak shift in the XRD pattern. Additionally, no extra peaks corresponding to impurities were observed in the XRD patterns of the powders, implying the appreciable purity of the synthesized powders. ICP data in Table 1 indicate a substitution rate of 5.44 mol% Zn in CSi, which is consistent with the expected value. The Na

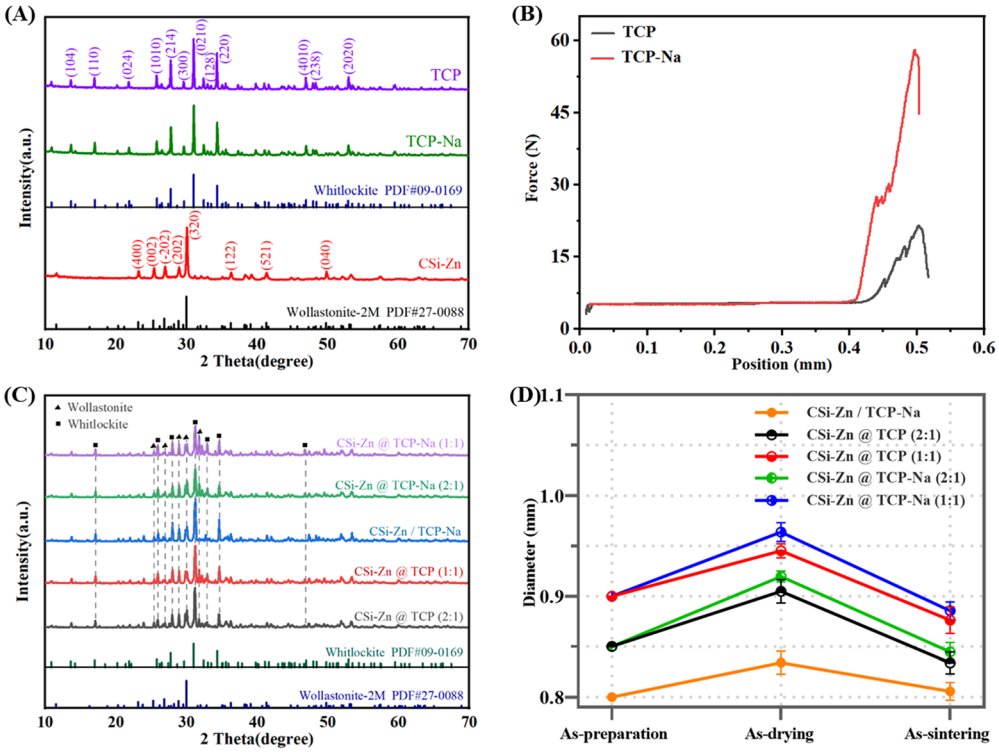

Fig. 2 Preliminary characterization of bioceramic powders and granules. (A) XRD patterns of the synthesized powders. (B) Force-position (*N*, mm) curves of TCP–Na and TCP powders. (C) XRD patterns of sintered core–shell bioceramic granules. (D) Diameter variation in bioceramic granules.

Table 1 Ionic percentage of powders detected through ICP-OES

Powders	Ca (ppm)	Si (ppm)	Zn (ppm)	P (ppm)	Na (ppm)	Zn replace Ca (%)	Na incorporation (%)
CSi–Zn	30.48	20.94	2.86	0	0.18	5.44	—
TCP	39.85	0	0	21.37	0.01	—	0.01
TCP–Na	38.07	0	0	20.45	0.25	—	0.25

content in TCP–Na reaches up to 0.25 mol%, confirming successful Na doping.

As illustrated in Fig. 2(B), the doping of Na indeed enhanced the sintering property (compressive resistance) of TCP, with TCP–Na exhibiting more than twice the compressive strength of pure TCP. After high-temperature sintering in a muffle furnace, Sudan III was volatilized, resulting in the core and shell colors becoming more uniform, although a distinct core–shell structure could still be observed macroscopically. It was seen from the XRD patterns (Fig. 2(C)) that the phase compositions of the core and shell components were well retained and the sintered core–shell granules were composed of wollastonite and whitlockite; it is evident that the chelated Mg ions from the collecting solution were doped into the structure of TCP, but not as the situation that the Ca ions would triggered TCP-to-HA phase transformation if Ca salt solution was used as fiber collecting medium. Moreover, the granule size varied at different stages accompanied by the thermal treatment. That is, the granule diameter showed an initial increase followed by a decrease during the preparation, drying, and sintering processes. The sintered granule size for the five different granules was 0.85 ± 0.05 mm, with minimal variation (Fig. 2(D)). Indeed, the granules with a core/shell thickness ratio of 1 : 1 were larger than those with a ratio of 2 : 1, and the granules with TCP–Na as the shell had slightly larger diameters than those with TCP shells. Interestingly, the mechanically mixed group had the smallest granule diameter.

3.2 Microstructure observation

Fig. 3(A)–(E) displays the SEM-observed microstructures on the fracture surface of core–shell granules. The core and shell layers can be distinguished based on grain morphology and core–shell interface. Unlike other core–shell granules, CSi–Zn/TCP–Na granules did not exhibit a visible core–shell feature because both the core and shell consisted of a biphasic mixture of CSi–Zn and TCP–Na with identical grain morphologies. EDS mapping (Fig. 3(F)–(J)) showed the distribution of Na, Mg, P, Si, and Zn elements in the fracture surface of granules. As expected, these elements were uniformly distributed in the CSi–Zn/TCP–Na granules. While in the other four groups, P and Si elements were predominantly distributed in the shell or core layers, respectively. Since CSi–Zn requires $Na_2SiO_3{\cdot}9H_2O$ in the

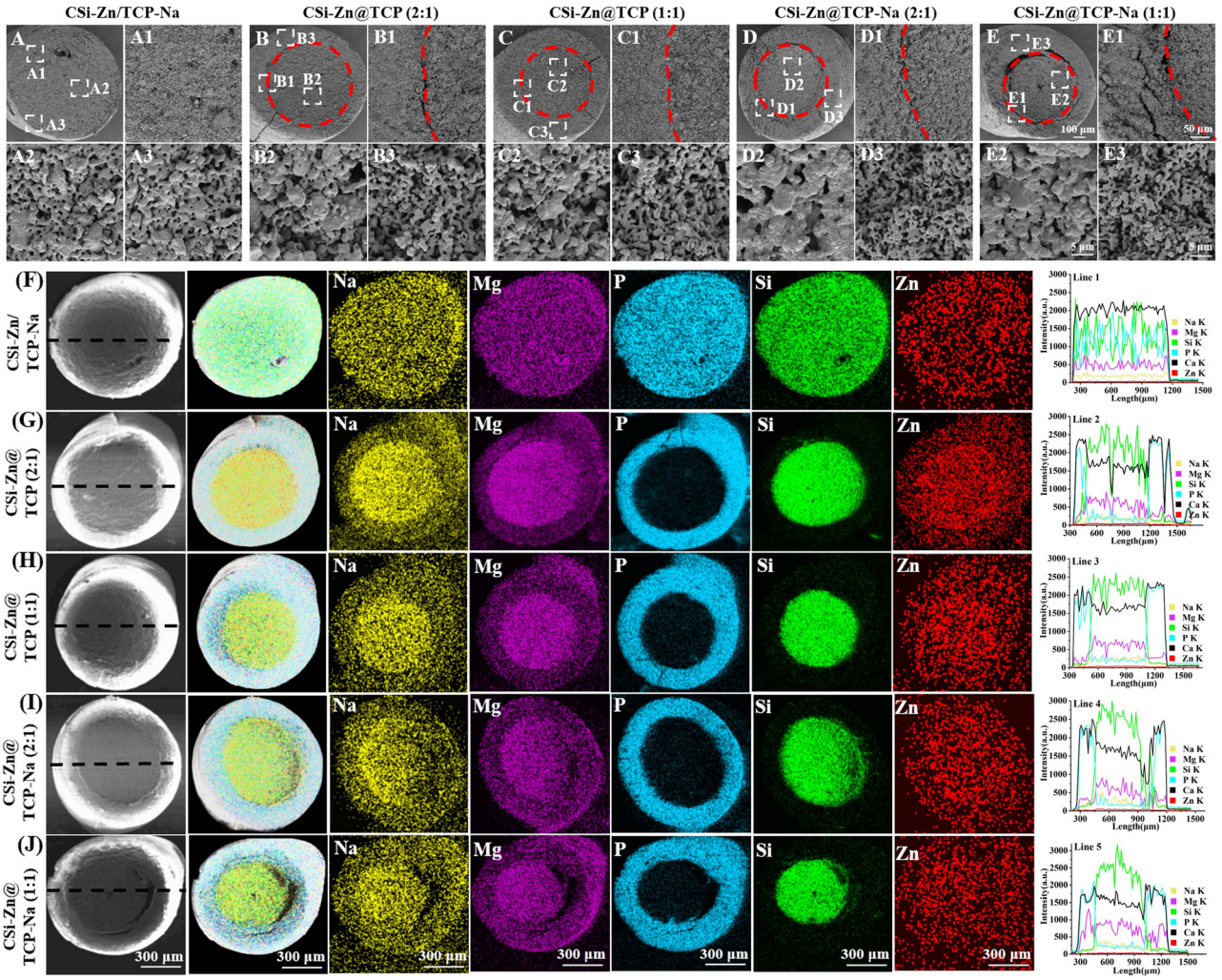

Fig. 3 SEM microstructure and EDS analysis of bioceramic granules. (A)–(E) Microstructure of sintered core–shell bioceramic granules, with the red dashed lines indicating the boundary between the core and shell layers. (F)–(J) EDS mapping and line scan spectra of the cross-sections of bioceramic granules.

preparation process, there is residual Na element in the core layer. In the early stage of the preparation process of core–shell slurry fibers, the precursors of bioceramic granules, which were not fully shaped after extrusion from the nozzle, need to be immersed in a magnesium salt solution for 12 hours, leading to some ion exchange between the fibers and the aqueous solution as well as between the core and shell materials. As the fibers were cut into granules, there was a chance for core and shell materials to cross into each other's regions. Consequently, Zn was detected in the shell layer in the EDS mapping of the granule cross-sections. EDS line scan data demonstrated the concentration of ions across the granule cross-section, with noticeable fluctuations in P and Si concentrations across different regions, consistent with the EDS mapping results.

3.3 *In vitro* biodegradation and re-mineralization

As shown in Fig. 4(A), the core–shell granules were immersed in a Tris buffer solution at 37 °C to simulate *in vivo* biodegradation. Fig. 4(B) shows that, in the early stages (0–1 week), the degradation rates of the five groups were similar to each other. However, the degradation rate of the mechanically mixed group gradually slowed compared to the core–shell structured groups with the prolongation of the immersion time. The degradation curves of the four core–shell groups largely overlapped during the initial four weeks. Although some differences emerged later, they remained relatively consistent.

Regarding ion release (Fig. 4(C)–(H)), all ions exhibited the fastest release rate after one day of immersion, followed by different degrees of slowing down. Ca and Si ions showed rapid release rates within 14 days, which then slowed down. Due to the doping of Na, which probably inhibits the TCP degradation, the concentration of Ca ions in granules with TCP–Na shells was lower than that in the granules with TCP shells (Fig. 4(C)). Core–shell granules with a core/shell thickness ratio of 2 : 1 had a higher proportion of core material than those with a ratio of 1 : 1. As Si ions were primarily released from the core layer, their concentration in the release curve (Fig. 4(D)) was higher for the former than for the latter. For the mechanically mixed

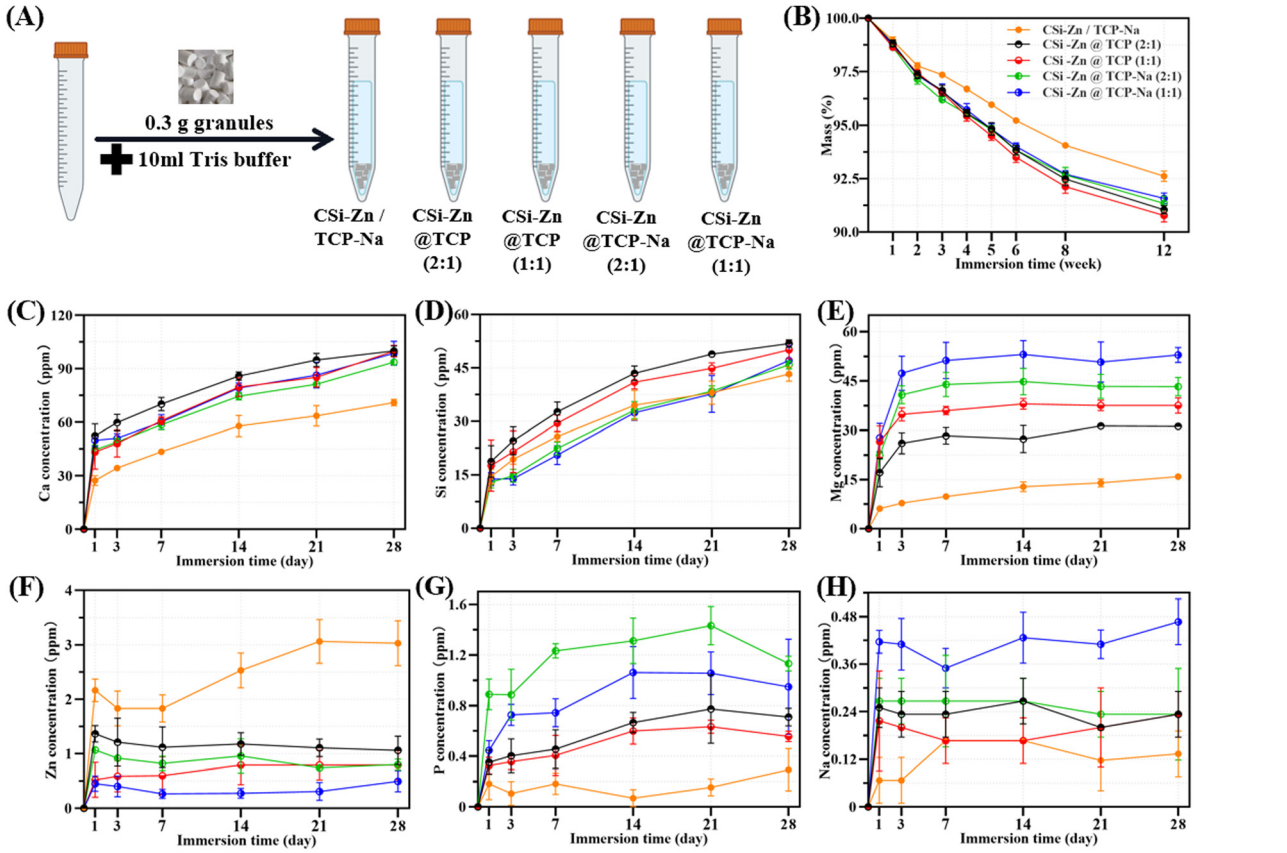

Fig. 4 Dissolution of core–shell granules *in vitro* in Tris buffer solution. (A) Schematic of the mass loss experiment for bioceramic granules. (B) Mass loss of granules. (C) Variation in the Ca concentration over time. (D) Variation in the Si concentration over time. (E) Variation in the Mg concentration over time. (F) Variation in the Zn concentration over time. (G) Variation in the P concentration over time. (H) Variation in the Na concentration over time.

CSi–Zn/TCP–Na group, where CSi was uniformly distributed, the Si release rate was similar to that of CSi–Zn@TCP–Na (2 : 1) and CSi–Zn@TCP–Na (1 : 1) granules, but consistently slower than that of CSi–Zn@TCP granules, implying that Na doping may retard the degradation of TCP. As shown in Fig. 4(E), Mg ions successfully retained in the core–shell granules were rapidly released within the initial three days. The rapid release behavior for Zn, P, and Na ions occurred only on the first day of immersion. As for Zn ions (Fig. 4(F)), in the core–shell structure group, they are mainly released from the core layer. As a result, granules with a core–shell thickness ratio of 2 : 1 exhibit higher release concentrations than those with a ratio of 1 : 1. In the mechanically mixed group, since CSi is uniformly distributed throughout the entire granule, Zn ions can still slowly release over 28 days. However, for the core–shell structure group, more time was needed for further degradation of the material before Zn in the core layer could continue to be released. Regarding the release of P element (Fig. 4(G)), its presence in TCP is mainly in the form of phosphate ions, with a relatively low amount of free P elements, resulting in a low release concentration. The same applies to Na element (Fig. 4(H)), where the initial low doping amount leads to a lower release concentration. Once Na^+ on the surface dissolves, a period of degradation is required before Na in the inner layers can be released again.

The granules were immersed in SBF for 1 and 2 weeks, and after washing and drying, their ability to induce Ca–phosphate re-mineralization *in vitro* was observed using SEM and EDS. As shown in Fig. 5, the cross-sectional surfaces of the granules exhibited the typical sintered grain interface and densification before immersion. After 1 week of immersion, the surface all became rough, containing some newly deposited granules. Images obtained at high magnification revealed the presence of microsphere aggregations resembling apatite on the granule surfaces. After 2 weeks, the aggregated microspheres became more pronounced. At this stage, even with a lower magnification than the observations made at 1 week, clear microsphere aggregations could still be observed. Furthermore, compared to TCP, the TCP–Na showed fewer deposited microspheres on its surface, and CSi–Zn/TCP–Na also showed fewer aggregates than the core–shell structure groups. The calcium-to-phosphorus (Ca/P) ratio on the granule surface after 2 weeks of immersion was measured using EDS. As shown in the spectra and quantitative analysis, the Ca/P ratio ranged from 1.80 to 2.63, implying a favorable apatite coverage on the granule surfaces. Of course, the Ca/P ratio being close to 1.5 is also related to

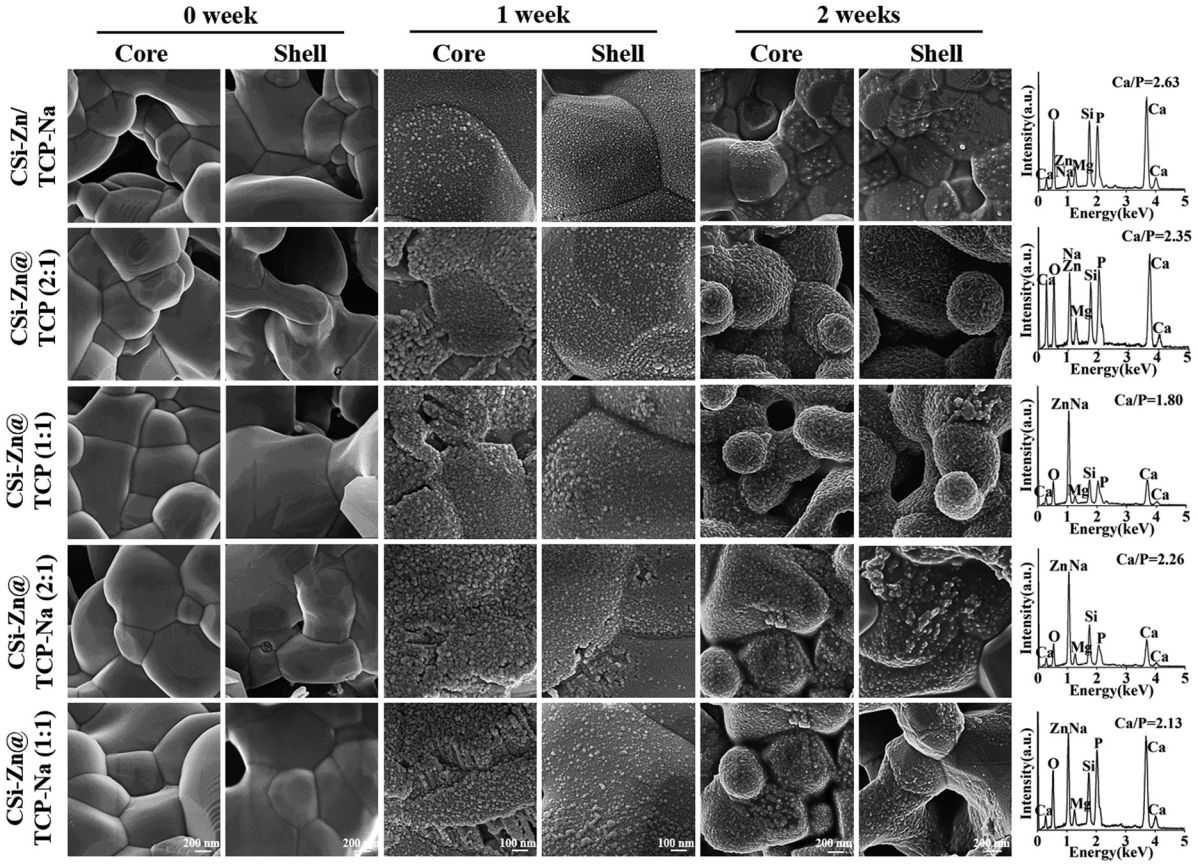

Fig. 5 SEM observations and EDS analyses of bioceramic granules after immersion in SBF for different time periods.

the fact that the shell layer used for the granules was TCP or TCP–Na.

3.4 Animal experiment evaluation

3.4.1 X-ray. Fig. 6(A) shows the animal experiment process, where approximately 0.17 g of core–shell granules were filled into each bone defect (∅6 mm × 7 mm). Specimens were collected for X-ray imaging and μCT analysis after 8 and 18 weeks of implantation, respectively. At 8 weeks, the implants were slightly degraded, and the boundary between the biomaterial and the host bone could be identified from the X-rays (Fig. 6(C)). After 18 weeks, the bone defect area appeared more indistinct, indicating ongoing material degradation and new bone tissue formation. This was corroborated by the specimen images (Fig. 6(B)), which showed more material residues at 8 weeks in comparison with the significantly fewer residues at 18 weeks.

3.4.2 μCT reconstruction analysis. As shown in Fig. 7(A), the 3D μCT-reconstructed images clearly demonstrated the core–shell structure of the granules. After 18 weeks of implantation in the rabbit, the granules in all experimental groups had not completely biodegraded. New bone grew from the outside to the inside of the closely packed granule systems, gradually filling the spaces between the granules and the voids left by granule degradation. The osteogenic effect of the core–shell granule groups was superior to that of the mechanically mixed group, proving the potential advantage of the core–shell structure design. The ratio of core-to-shell components was also critical for new bone ingrowth, as shown in Fig. 7(A), and the granules with a thickness ratio of 1/1 had better osteogenic capability than those with a ratio of 2/1 at both short (8 weeks) and long (18 weeks) intervals.

At 8 weeks, the granules with TCP shells showed more fragmentation and core–shell separation than those with TCP–Na shells. This is another proof of the enhancing effect of Na element on the sintering properties of TCP. In terms of osteogenesis, TCP–Na was less effective than pure TCP due to its higher biological stability. Over time, the CSi–Zn@TCP (2 : 1) and CSi–Zn@TCP (1 : 1) granules were degraded, allowing more space for new bone tissue ingrowth, whereas the other two groups, CSi–Zn@TCP–Na (2 : 1) and CSi–Zn@TCP–Na (1 : 1), showed slower degradation and less new bone formation, as in the mechanically mixed group.

Fig. 7(B) presents the quantitative data on residual material volume fraction (RV/TV), bone volume fraction (BV/TV), and mean trabecular number (Tb.N). From 8 to 18 weeks, the BV/TV of CSi–Zn@TCP (2 : 1) and CSi–Zn@TCP (1 : 1) was significantly increased, and both groups also had higher trabecular numbers than the other three groups at both intervals. The RV/TV, BV/TV, and Tb.N data sometimes showed no significant differences between CSi–Zn@TCP–Na (2 : 1) and CSi–Zn@TCP–Na (1 : 1) groups.

3.4.3 Histological analysis. H&E staining and Masson trichrome staining images (Fig. 8) indicated that bone tissue grew

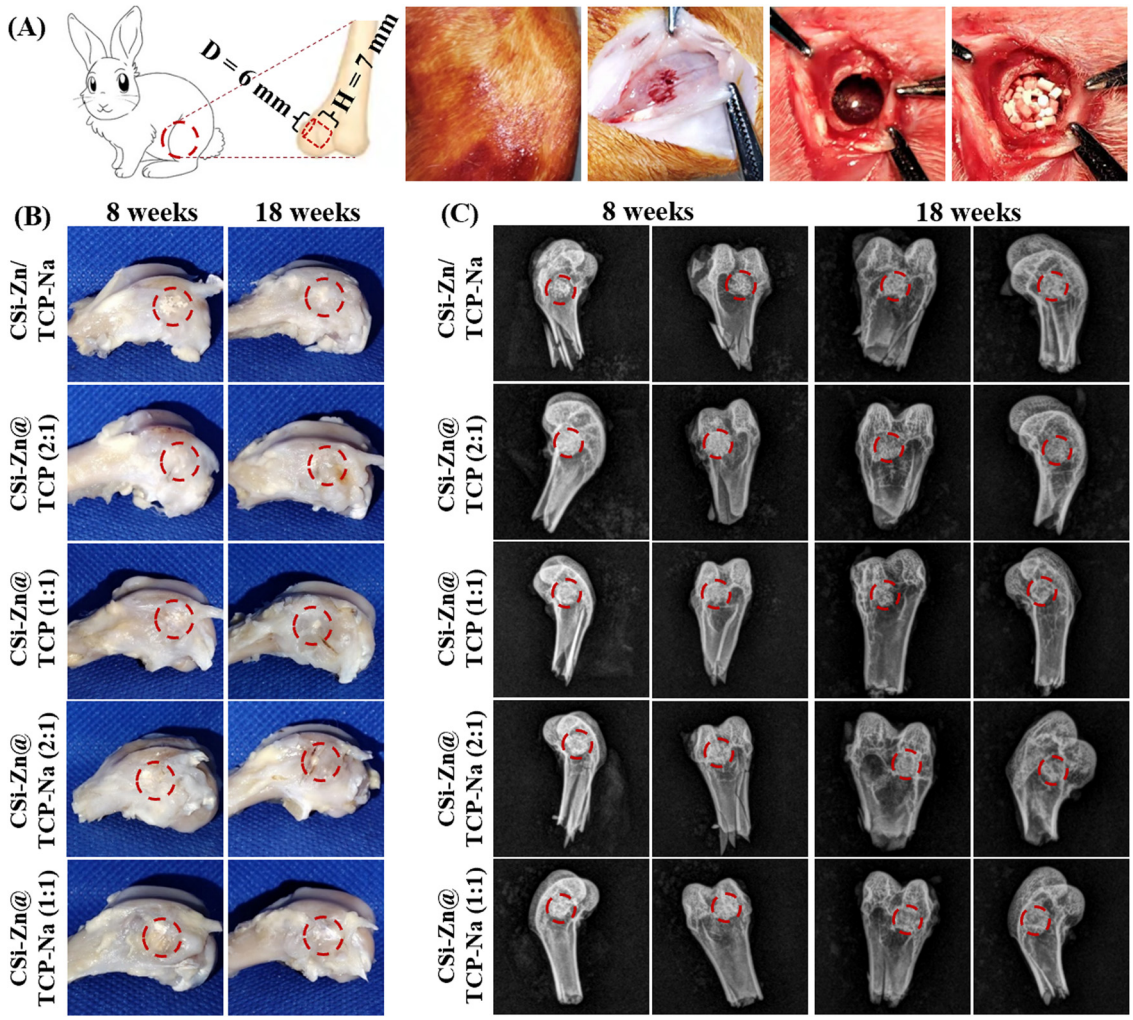

Fig. 6 Animal experiments and preliminary analysis of the results. (A) Schematic of the femoral defect model and animal surgery process. (B) Femoral specimens collected at 8 and 18 weeks. (C) X-ray images of femoral specimens at 8 and 18 weeks.

along the gaps between granules and gradually occupied the voids released by material biodegradation. At 8 weeks, CSi–Zn@TCP (2 : 1) and CSi–Zn@TCP (1 : 1) groups had significantly more new bone tissue formation than the other three groups, demonstrating their superior early-stage osteogenic capability. The mechanically mixed group showed minimal new bone formation around the granules, indicating the poor early osteoconductive potential. Over time, as the granule biomaterials degraded, all four core–shell structured groups exhibited separation between core and shell layers. From 8 to 18 weeks, the amount of mature bone tissue increased in all groups, consistent with the quantitative analysis data in Fig. 7. The quantitative analysis results of BS/TS in Fig. 9 also supported this observation.

4. Discussion

Bone defects exceeding the critical size can be caused by various factors such as external trauma and internal tumor growth. The self-repair capability of bone is limited, and without artificial intervention, it may affect the patient's quality of life, potentially leading to disabilities or triggering other diseases. Not all natural or artificial materials are suitable for bone grafting. The biocompatibility, cytocompatibility, and biological functionality of the implants are crucial considerations. In general, it is well agreed that the biodegradation of the material should ideally be synchronized with new bone regeneration to ensure continuous and stable support before the new bone tissue fully forms. Hence, the common route is to prepare the biphasic composites or foreign ion doping bioceramics to improve some physicochemical properties or biological performances.

It is known that some Ca–silicate and -phosphate ceramic materials are commonly studied candidates in bone tissue engineering, each with its own advantages and disadvantages. The most prospective materials for bone regeneration today are almost exclusively composites comprising two or more components that compensate for the shortcomings of each one of them alone. However, the design of bi- or multi-component composites to overcome and even improve ('1 + 1 > 2') the

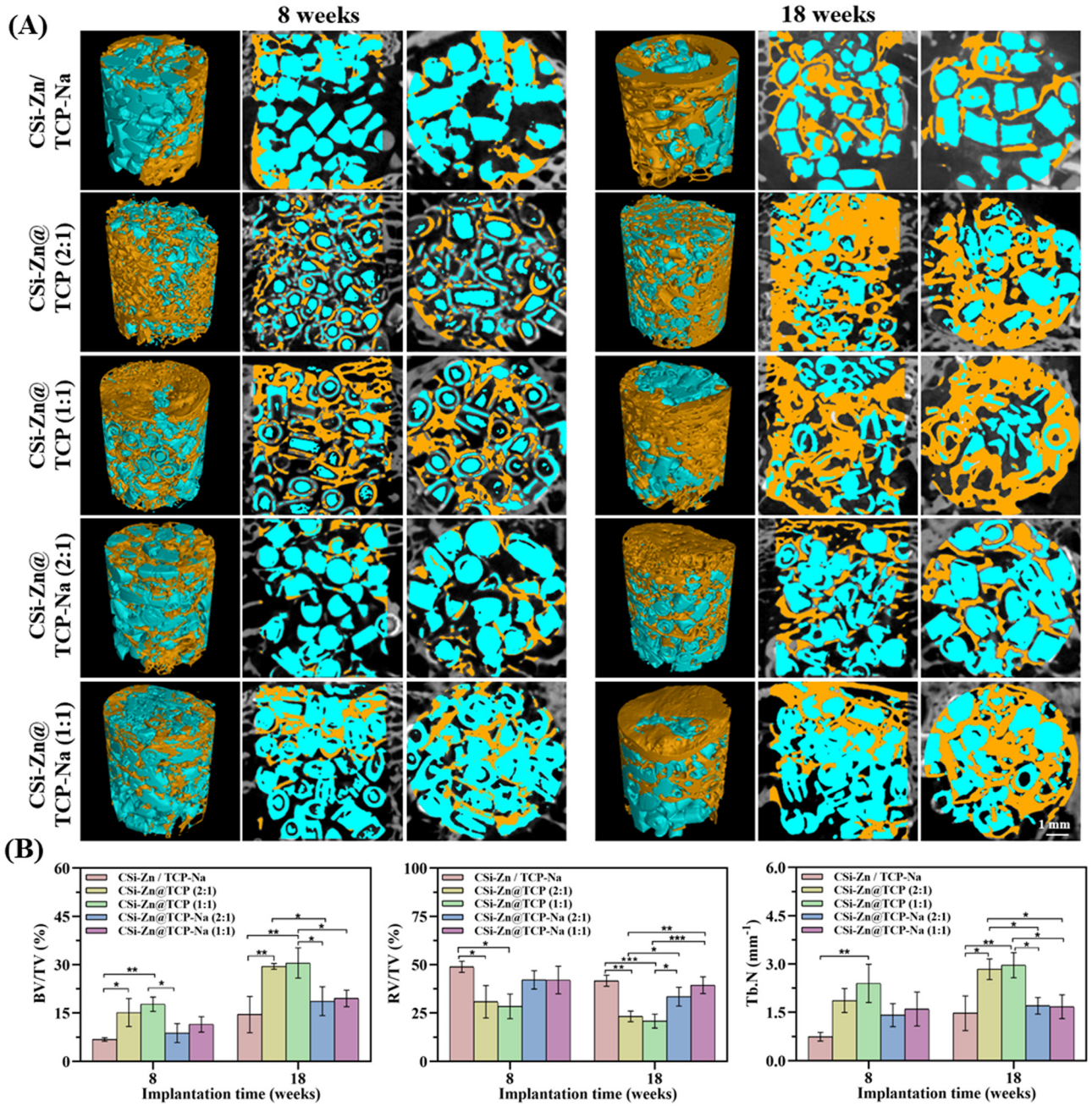

Fig. 7 Micro-CT reconstruction and analysis of femoral specimens. (A) 2D and 3D reconstruction images of bioceramic granules filling femoral defects at 8 and 18 weeks. (B) Quantitative analysis of RV/TV, BV/TV, and Tb.N. $N = 3$; $^{*}P < 0.05$, $^{**}P < 0.01$, $^{***}P < 0.001$. Green: material; yellow: new bone tissue.

shortcomings of single bioceramics is still a challenge.[50] In this aspect, the present study aimed to explore the bone regeneration capacity of combining these two typical biomaterials in a core–shell structure with varying thickness ratios and Zn and Na ion dopings. In particular, to address the potential shortcomings, the dissolvable Mg salt solution was used to collect the slurry fibers to avoid the TCP-to-HA phasic conversion in the shell layer.

Zn ions, being divalent cations with an ionic radius slightly smaller than that of Ca ions, can replace some Ca sites when Zn is incorporated into CSi, causing lattice contraction. At the same time, the doping of Zn can reduce crystal defects and improve the integrity of the lattice, among other things. Furthermore, Zn possesses broad-spectrum antibacterial properties. Thus, doping CSi with an appropriate amount of Zn not only improves the sintering properties but also endows it with the antibacterial capability,[51,52] and in fact Zn is also essential for normal bone growth and development.[53] Regarding Na doping, various *in vitro* and *in vivo* tests in this study have confirmed its role in improving the sintering and densification

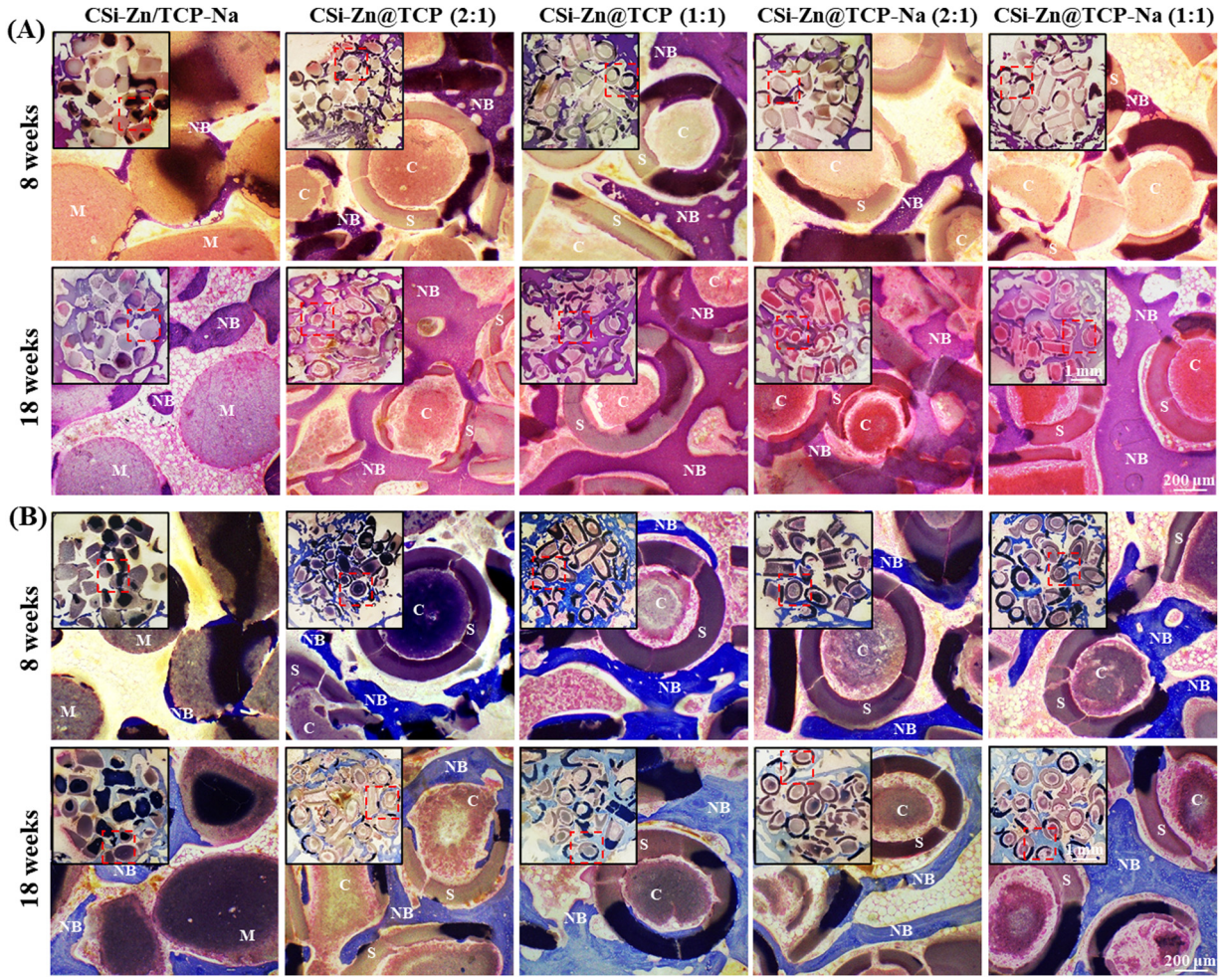

Fig. 8 H&E staining (A) and Masson trichrome staining (B) analysis of bioceramic granules implanted in femoral defects at 8 and 18 weeks. NB: new bone tissue; M: material; C: core material, CSi–Zn; S: shell material, TCP or TCP–Na.

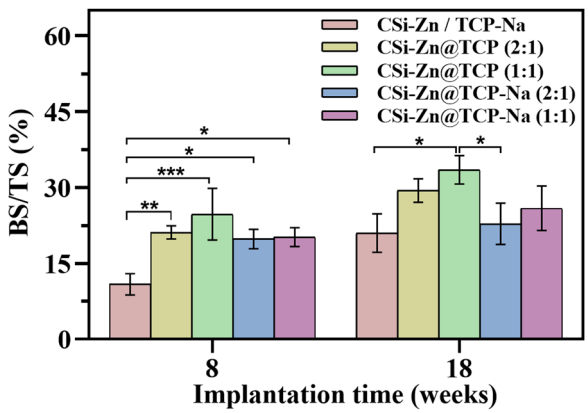

Fig. 9 Quantitative analysis of BS/TS for bioceramic granule implantation in femoral defects was performed based on H&E staining images. $N = 3$; $^{*}P < 0.05$, $^{**}P < 0.01$, $^{***}P < 0.001$.

and inhibiting biodegradation behavior of TCP, which is consistent with the experimental results of Obadia *et al.*[44] Unfortunately, under the experimental biphasic composite conditions in the present study, the Na-doped granules did not exhibit appreciable osteogenic advantage. As shown in the micro-CT images in Fig. 7, the osteogenic efficiency of the core–shell granules with the TCP–Na shell was inferior to that of granules with the TCP shell. Combined with the quantitative data of BV/TV and RV/TV, and the analysis of granule degradation and ion release in Fig. 4, this is mainly attributed to the slow biodegradation of the TCP–Na shell component, leading to a mismatch between the bone tissue ingrowth and material biodegradation. In this regard, our previous studies have indicated that the TCP-to-HA phase conversion would inhibit the biodegradation of the biphasic composites,[45] and thus, the enhancement of osteogenic capability needs high-density microspheres in the shell component.[54] Therefore, future studies using Na doping strategies might consider endowing a certain amount of microspheres in the TCP–Na shell layer to provide higher specific surface areas and these microporous structures would be beneficial for the bio-dissolution of the CSi–Zn core component through shell coating and body fluid infiltration, thereby better promoting osteogenesis.

Furthermore, it is well known that cell adhesion to material surfaces relies on integrin signaling. Mg ions promote integrin expression, enhancing the adhesion, proliferation, and differentiation of osteoblasts,[55,56] thereby promoting bone tissue growth in a better way. Therefore, unlike previous studies[57,58] that used a calcium nitrate solution, this study utilized magnesium nitrate as the receiving solution, leveraging Mg^{2+} to chelate with CC and CMC to maintain the slurry fibrous morphology. This strategy not only introduces a new ion with osteogenic properties but also avoids the potential negative effects of high Ca content, which may lead to phase transformation. Mg, like Ca, is an essential metal element in the human body, with many physiological activities depending on Mg, and bones containing 50–60% of the body's Mg. In order to optimize the composition in the shell layer and fiber stability, we carefully controlled the concentration of magnesium salts in the receiving liquid, ensuring sufficient Mg^{2+} for chelation. This approach helped to stabilize the fiber morphology, ensuring more uniform granule diameters in the cut bioceramic granules, while also preventing the potential negative effects of excessive magnesium ion concentrations. The successful execution of the experiment and the Mg ion release data in Fig. 4 demonstrate the feasibility of this strategy. That is, this method also has a degree of versatility, with Mg^{2+} replaceable by or combinable with other ions to form new receiving solutions.

Moreover, this study introduced a traditional mechanical mixing group for comparative experiments. Mass loss and ion release profiles indicate a correlation between ion release and material degradation. Compared to the core–shell structure group, the mechanically mixed group exhibited the slowest mass loss rate, with corresponding slower release rates of Ca, Mg, P, and Na. However, because the components in the mechanically mixed group were uniformly distributed, unlike the core–shell structure group where the CSi core layer is partially enclosed by the TCP shell, the release of Si ions was not slower than that of the core–shell structure groups with TCP–Na cores, and even the concentration of Zn ions released within 28 days was higher than that of the other four groups. Nonetheless, animal experiments demonstrated that this uniform mixing approach was not ideal, as the osteogenic efficiency in the mechanically mixed group was significantly lower than that in the core–shell groups, both in the early (8 weeks) and late (18 weeks) stages. Previous studies have still investigated bioceramic microspheres with similar core–shell structures.[45–48] However, such bioceramic microsphere structures enclose the entire core component layer within the shell, tightly linking the core's degradation rate to that of the microstructures of the shell layer. If the shell degrades slowly, the core components may remain unreleased for extended periods. Separating the two components into distinct core and shell layers allowed for more controllable biodegradation behavior in comparison with the mechanically mixed group. Furthermore, this approach allows the core layer to degrade and release independently of the shell layer to some extent, enabling better synergistic action between the two components, which may be more beneficial for bone tissue ingrowth. The as-cut fibers would expose the core component layer in the two fracture surface, and thus the CSi–Zn core component with high osteogenic activity would accelerate the new bone growth and fibro-vascularization in the early stage after implantation. Additionally, we consciously controlled the thickness ratio between the core and shell layers, exploring the osteogenic effects under two different thickness ratios. The differences in thickness can be observed through surface scanning and line scanning images of several granules (Fig. 3). Experimental results show that core–shell granules with a radius ratio of 1/1 exhibit better osteogenic effects at both early (8 weeks) and late (18 weeks) stages compared to those with a ratio of 2/1. Consistent with this observation, our previous study[57] also demonstrated that the 1 : 1 core–shell thickness ratio resulted in better osteogenic outcomes than the other ratios. These new findings show the necessity and feasibility of precisely controllable or tailorable potential of the thickness ratio of the core–shell bioceramic fiber structure. The optimal thickness ratio for this material combination remains yet to be determined. More detailed and long-term experiments are required to further optimize and validate this, to better suit the filling and repair of various bone defects in the future.

In bone regenerative medicine, porous scaffolds are the indispensable structure and functional units, with the material volume matching the bone defect cavity.[59] To meet the requirements of cell adhesion, proliferation, and differentiation, further promoting angiogenesis and osteogenesis, porosity is a critical factor to consider. The size, volume, and interconnectivity of pores influence cell proliferation, differentiation, and new bone tissue formation.[60] This presents an advantage in our research. In the early stages when the granule materials have not yet begun to degrade, porosity mainly comes from the gaps between the closely packed granule systems, meaning that it is completely interconnective and controllable. This certainty might be favorable for vascularization and enhancing final bone repair outcome. Therefore, the design and application of selectively ion-doped core–shell bioceramic granule materials still require promising refinement and optimization to reliably adapt to bone defect repairs in various scenarios. Altogether, it is reasonable to consider that this scheme is highly adaptable, allowing for the customization of various bioceramic combination strategies to develop various granule-typing biomaterial implants for some different bone defect conditions.

5. Conclusions

In summary, this study provides a new strategy to prepare core–shell bioceramic granules with different components, thickness ratios and/or ion dopings based on CSi and TCP raw materials, two typical bioactive candidates with different biodegradation features. Compared to the conventional mechanical mixing route, all four groups of core–shell bioceramic granules exhibited tunable biodegradation and bone repair capabilities. Additionally, minor doping of foreign ions altered the biodegradation and ion release rates of the core and shell materials, further influencing the bone regeneration and repair

process. Altogether, it is reasonable to consider that the CSi–Zn@TCP bioceramic granules with a core–shell radius ratio of 1/1 demonstrate a more ideal biodegradation behavior and osteogenic efficiency, making them expected implants for bone defect repair.

Data availability

The data supporting this study are included in the article; further inquiries can be directed to the corresponding author/s.

Conflicts of interest

The authors declare that they have no conflict of interests.

Acknowledgements

The authors would like to acknowledge financial support from the Zhejiang Provincial Natural Science Foundation of China (LZ22E020002), Key Laboratory of Oral Biomedical Research of Zhejiang Province Foundation (2021M001), Zhejiang Provincial Basic Research for Public Welfare Funds (LGF22E030002, LGF21H060006) and National Natural Science Foundation of China (82101649).

References

1 A. Salhotra, H. N. Shah, B. Levi and M. T. Longaker, *Nat. Rev. Mol. Cell Biol.*, 2020, **21**, 696–711.
2 R. Marsell and T. A. Einhorn, *Injury*, 2011, **42**, 551–555.
3 J. P. Schmitz and J. O. Hollinger, *Clin. Orthop. Relat. Res.*, 1986, 299–308.
4 P. G. Robinson, G. D. Abrams, S. L. Sherman, M. R. Safran and I. R. Murray, *Oper. Tech. Sports Med.*, 2020, **28**, 150780.
5 E. M. Younger and M. W. Chapman, *J. Orthop. Trauma*, 1989, **3**, 192–195.
6 J. Baumhauer, M. S. Pinzur, R. Donahue, W. Beasley and C. DiGiovanni, *Foot Ankle Int.*, 2014, **35**, 104–107.
7 V. Campana, G. Milano, E. Pagano, M. Barba, C. Cicione, G. Salonna, W. Lattanzi and G. Logroscino, *J. Mater. Sci.: Mater. Med.*, 2014, **25**, 2445–2461.
8 U. Kneser, D. J. Schaefer, B. Munder, C. Klemt, C. Andree and G. B. Stark, *Minim. Invasive Ther. Allied Technol.*, 2002, **11**, 107–116.
9 A. J. Salgado, O. P. Coutinho and R. L. Reis, *Macromol. Biosci.*, 2004, **4**, 743–765.
10 A. R. Amini, C. T. Laurencin and S. P. Nukavarapu, *Crit. Rev. Biomed. Eng.*, 2012, **40**, 363–408.
11 G. Harini, R. Bharathi, A. Sankaranarayanan, A. Shanmugavadivu and N. Selvamurugan, *Mater. Adv.*, 2023, **4**, 3907–3928.
12 A. Atala, F. K. Kasper and A. G. Mikos, *Science Transl. Med.*, 2012, **4**, 160rv12.
13 P. Piste, D. Sayaji and M. Avinash, *Int. J. Res. Pharm. Biomed. Sci.*, 2012, **4**, 2229–3701.
14 E. O'Neill, G. Awale, L. Daneshmandi, O. Umerah and K. W. Lo, *Drug Discovery Today*, 2018, **23**, 879–890.
15 M. Goretti Penido and U. S. Alon, *Pediatr. Nephrol.*, 2012, **27**, 2039–2048.
16 S. Khoshniat, A. Bourgine, M. Julien, P. Weiss, J. Guicheux and L. Beck, *Cell. Mol. Life Sci.*, 2011, **68**, 205–218.
17 A. S. Prasad, *Nutrition*, 1995, **11**, 93–99.
18 E. M. Carlisle, *Science*, 1970, **167**, 279–280.
19 A. F. Khan, M. Saleem, A. Afzal, A. Ali, A. Khan and A. R. Khan, *Mater. Sci. Eng., C*, 2014, **35**, 245–252.
20 P. Valerio, M. M. Pereira, A. M. Goes and M. F. Leite, *Biomaterials*, 2004, **25**, 2941–2948.
21 S. C. Huang, B. C. Wu and S. J. Ding, *J. Mater. Chem. B*, 2015, **3**, 570–580.
22 S. Nilawar, M. Uddin and K. Chatterjee, *Mater. Adv.*, 2021, **2**, 7820–7841.
23 M. Nasr Azadani, A. Zahedi, O. K. Bowoto and B. I. Oladapo, *Prog. Biomater.*, 2022, **11**, 1–26.
24 H. Shi, Z. Zhou, W. Li, Y. Fan, Z. Li and J. Wei, *J. Biomed. Mater. Res.*, 2021, **11**, 149.
25 F. Fendi, B. Abdullah, S. Suryani, I. Raya, D. Tahir and I. Iswahyudi, *Polym. Bull.*, 2024, **81**, 1097–1116.
26 T. Tanaka, H. Komaki, M. Chazono, S. Kitasato, A. Kakuta, S. Akiyama and K. Marumo, *Morphologie*, 2017, **101**, 164–172.
27 M. Bohner, B. L. G. Santoni and N. Döbelin, *Acta Biomater.*, 2020, **113**, 23–41.
28 X. Ye, Y. Zhang, T. Liu, Z. Chen, W. Chen, Z. Wu, Y. Wang, J. Li, C. Li, T. Jiang, Y. Zhang, H. Wu and X. Xu, *Int. J. Biol. Macromol.*, 2022, **209**, 1553–1561.
29 F. Geng, L. Tan, B. Zhang, C. Wu, Y. He, J. Yang and K. Yang, *J. Mater. Sci. Technol.*, 2009, **25**, 123–129.
30 S. Ni, J. Chang and L. Chou, *J. Biomed. Mater. Res., Part A*, 2006, **76**, 196–205.
31 F. Yang, J. Lu, Q. Ke, X. Peng, Y. Guo and X. Xie, *Sci. Rep.*, 2018, **8**, 7345.
32 R. Kumar, I. Pattanayak, P. A. Dash and S. Mohanty, *J. Mater. Sci.*, 2023, **58**, 3460–3484.
33 S. Mofakhami and E. Salahinejad, *Coord. Chem. Rev.*, 2024, **514**, 215963.
34 Z. Wu, Z. Zhong, W. He, Y. Wu, Y. Cai, H. Yang and Y. Hong, *Mater. Adv.*, 2022, **3**, 4295–4309.
35 M. Cicuéndez, P. Portolés, M. Montes-Casado, I. Izquierdo-Barba, M. Vallet-Regí and M. T. Portolés, *J. Mater. Chem. B*, 2014, **2**, 3469–3479.
36 D. Shekhawat, A. Singh, M. K. Banerjee, T. Singh and A. Patnaik, *Ceram. Int.*, 2021, **47**, 3013–3030.
37 Q. Wu, X. Wang, F. Jiang, Z. Zhu, J. Wen and X. Jiang, *Int. J. Oral Sci.*, 2020, **12**, 25.
38 M. Sun, A. Liu, H. Shao, X. Yang, C. Ma, S. Yan, Y. Liu, Y. He and Z. Gou, *Sci. Rep.*, 2016, **6**, 34029.
39 J. Yu, L. Xu, K. Li, N. Xie, Y. Xi, Y. Wang, X. Zheng, X. Chen, M. Wang and X. Ye, *Sci. Rep.*, 2017, **7**, 3440.
40 Y. Ramaswamy, C. Wu, H. Zhou and H. Zreiqat, *Acta Biomater.*, 2008, **4**, 1487–1497.
41 D. Hu, K. Li, Y. Xie, H. Pan, J. Zhao, L. Huang and X. Zheng, *J. Mater. Sci.: Mater. Med.*, 2016, **27**, 56.

42 C. Wu, Y. Ramaswamy, J. Chang, J. Woods, Y. Chen and H. Zreiqat, *J. Biomed. Mater. Res., Part B*, 2008, **87**, 346–353.
43 L. Obadia, P. Deniard, B. Alonso, T. Rouillon, S. Jobic, J. Guicheux, M. Julien, D. Massiot, B. Bujoli and J. M. Bouler, *Chem. Mater.*, 2006, **18**, 1425–1433.
44 L. Obadia, M. Julien, S. Quillard, T. Rouillon, P. Pilet, J. Guicheux, B. Bujoli and J. M. Bouler, *J. Mater. Sci.: Mater. Med.*, 2011, **22**, 593–600.
45 X. Ke, C. Zhuang, X. Yang, J. Fu, S. Xu, L. Xie, Z. Gou, J. Wang, L. Zhang and G. Yang, *ACS Appl. Mater. Interfaces*, 2017, **9**, 24497–24510.
46 A. Xu, C. Zhuang, S. Xu, F. He, L. Xie, X. Yang and Z. Gou, *Sci. Rep.*, 2018, **8**, 3385.
47 C. Zhuang, X. Ke, Z. Jin, L. Zhang, X. Yang, S. Xu, G. Yang, L. Xie, G. E. Prince, Z. Pan and Z. Gou, *J. Mater. Chem. B*, 2017, **5**, 8944–8956.
48 L. Liu, D. He, X. Yang, L. Zhang, G. Yang, X. Dai and Z. Gou, *J. Am. Ceram. Soc.*, 2016, **99**, 2243–2252.
49 J. Xie, X. Yang, H. Shao, J. Ye, Y. He, J. Fu, C. Gao and Z. Gou, *J. Mech. Behav. Biomed. Mater.*, 2016, **54**, 60–71.
50 V. Uskoković, *Mater. Sci. Eng., C*, 2015, **57**, 434–451.
51 T. Lu, Y. Miao, T. Wu, J. Ye and Y. Zhang, *Ceram. Int.*, 2024, **50**, 17214–17227.
52 Y. Peng, M. Chen, J. Wang, J. Xie, C. Wang, X. Yang, X. Huang, Z. Gou and J. Ye, *Bioact. Mater.*, 2024, **36**, 551–564.
53 M. Yamaguchi, *J. Trace Elem. Exp. Med.*, 1998, **11**, 119–135.
54 J. Fu, C. Zhuang, J. Qiu, X. Ke, X. Yang, Z. Jin, L. Zhang, G. Yang, L. Xie, S. Xu, C. Gao and Z. Gou, *Tissue Eng., Part A*, 2019, **25**, 588–602.
55 H. Zreiqat, C. R. Howlett, A. Zannettino, P. Evans, G. Schulze-Tanzil, C. Knabe and M. Shakibaei, *J. Biomed. Mater. Res.*, 2002, **62**, 175–184.
56 Z. Shi, G. Huang, Z. Li, Z. Lou, Z. Gong, X. Wang, C. Li and B. Wang, *Mater. Adv.*, 2023, **4**, 3583–3592.
57 J. Shen, Y. Li, J. Li, M. Shen, Y. Xu, Y. Zhang, X. Yang, C. Wang, Z. Gou, S. Xu and S. Xu, *Mater. Des.*, 2024, **243**, 113054.
58 Z. Bao, J. Yang, J. Shen, C. Wang, Y. Li, Y. Zhang, G. Yang, C. Zhong, S. Xu, L. Xie, M. Shen and Z. Gou, *J. Mater. Chem. B*, 2023, **11**, 2417–2430.
59 C. Xu, Z. Liu, X. Chen, Y. Gao, W. Wang, X. Zhuang, H. Zhang and X. Dong, *Chin. Chem. Lett.*, 2024, **35**, 109197.
60 P. Yadav, G. Beniwal and K. K. Saxena, *Mater. Today: Proc.*, 2021, **44**, 2623–2628.